Watching energy transfer in metalloporphyrin heterodimers using stimulated X-ray Raman spectroscopy

Jason D. Biggs[1], Yu Zhang[1], Daniel Healion, and Shaul Mukamel[2]

Department of Chemistry, University of California, Irvine, CA 92697

Edited by Harry B. Gray, California Institute of Technology, Pasadena, CA, and approved August 6, 2013 (received for review May 7, 2013)

Understanding the excitation energy transfer mechanism in multiporphyrin arrays is key for designing artificial light-harvesting devices and other molecular electronics applications. Simulations of the stimulated X-ray Raman spectroscopy signals of a Zn/Ni porphyrin heterodimer induced by attosecond X-ray pulses show that these signals can directly reveal electron–hole pair motions. These dynamics are visualized by a natural orbital decomposition of the valence electron wavepackets.

chromophore aggregates | core transitions | REW-TDDFT | nonlinear

Porphyrin rings are pyrole-based cyclic conjugated systems that serve as the main building blocks in many devices that depend on their high excitation energy transfer (EET) efficiency (1–4). Because of their stability and interesting structural, electronic, and optical properties, porphyrin compounds have a wide range of uses as chemical sensors (5), photosensitizers in photodynamic therapy for cancer (6), nonlinear optical materials (7–9), and molecular electronic (10–12) and spintronic devices (13, 14).

Porphyrin-based molecules hold a pivotal position in the chemistry of engineered photoactive organic compounds, and extensive electronic structure calculations of monomeric (15) and oligomeric (16, 17) porphyrin molecules, porphyrin structures in biomacromolecules (18, 19), and quasi-1D and -2D porphyrin systems with infinite sizes have been carried out (13, 14, 20–23). Most applications involve multiporphyrin arrays, either in linear or in cyclic shape, or dendrimers (24). Porphyrin dimers, which are still small enough to be treated with relatively high-level modern quantum chemistry methods, can offer basic clues to track down the more complicated EET dynamics in multiporphyrin arrays.

The kinetics of EET in multiporphyrin systems have long been studied by time-resolved fluorescence anisotropy decay (25) and pump–probe techniques, using visible light (26).

Here we present a simulation study that shows how recently developed attosecond sources of X-ray pulses may be used to probe the energy transfer dynamics in a porphyrin dimer. Intense attosecond X-ray pulses, recently made available by new X-ray free electron laser (XFEL) (27, 28) and higher harmonic generation (29, 30) sources, have bandwidths covering multiple electron volts and can prepare coherent superpositions of valence electronically excited states through an impulsive Raman process (31). The short durations of these pulses make them ideal for tracing valence electronic dynamics that evolve with extremely short periods. X-ray pulses can also exploit the spectrally isolated core-excitation frequencies to create valence excitations in the neighborhood of a selected atom, a type of localized excitation not generally accessible using visible or UV pulses. An experimental realization of a two-color pump–probe X-ray source from XFEL radiation was recently reported (32). These new sources have also been used in time-dependent X-ray diffraction studies (33), to monitor ultrafast changes in the conductivity of semiconductors (34) and measure metal-to-ligand charge transfer in inorganic complexes (35) and the ultrafast dissociation of molecules adsorbed on a metal surface (36). Many of these techniques use the X-ray light source only for the probing pulse (37, 38) or depend on a detection method relying on ion or electron capture after the molecule interacts with the X-rays (39). All-X-ray photon-in, photon-out measurements are experimentally very difficult, and X-ray pump–probe measurements with attosecond pulses have yet to be performed. A series of theoretical studies on the time-domain, impulsive X-ray Raman signals of small organic molecules at the K-edges of second- and third-row elements have explored some of the unique capabilities of this technique (31).

The porphyrin ring can chelate different metal atoms, changing the properties of the chromophore. This variability makes porphyrin systems ideal candidates for stimulated X-ray excitation; the spectrally isolated core transitions of the central metal atom allow them to act as X-ray dyes, creating local excitations through an X-ray Raman process.

In this paper we simulate the stimulated X-ray Raman spectroscopy (SXRS) signals of a Zn-Ni porphyrin dimer linked by an ethynyl group. A natural orbital analysis (40, 41) of the electronic wavepacket that evolves during the delay between pulses is used to characterize the electron and hole dynamics after excitation.

Stimulated X-Ray Raman Spectroscopy

Stimulated X-ray Raman spectroscopy uses ultrashort X-ray pulses to probe valence excitations. In this technique, the system is excited by a pump pulse and the transmission of the probe pulse is recorded after a delay τ (31). Each pulse interacts with the system twice via a stimulated Raman process. A core electron is excited into an unoccupied orbital during each pulse; the excited system then evolves for a short period in the core-excited state before a second interaction with the same pulse stimulates a valence electron to destroy the core hole, emitting an X-ray photon in the process. The system is left in a coherent superposition of valence-

Significance

Energy transfer in multiporphyrin arrays is of fundamental interest and plays an important role in natural and artificial light harvesting. In this work, we show how ultrafast hard X-ray pulses may be used to create localized electronic wavepackets in a metalloporphyrin dimer. Energy migration between monomers is detected through a stimulated Raman process, resonant with the metal core. Combining the broad bandwidth of attosecond pulses with the localized nature of core orbitals results in a much higher degree of localization and temporal resolution than is possible with optical pulses.

Author contributions: J.D.B., Y.Z., and S.M. designed research; J.D.B., Y.Z., and D.H. performed research; J.D.B., Y.Z., and D.H. analyzed data; and J.D.B., Y.Z., D.H., and S.M. wrote the paper.

The authors declare no conflict of interest.

This article is a PNAS Direct Submission.

[1]J.D.B. and Y.Z. contributed equally to this work.

[2]To whom correspondence should be addressed. E-mail: smukamel@uci.edu.

This article contains supporting information online at www.pnas.org/lookup/suppl/doi:10.1073/pnas.1308604110/-/DCSupplemental.

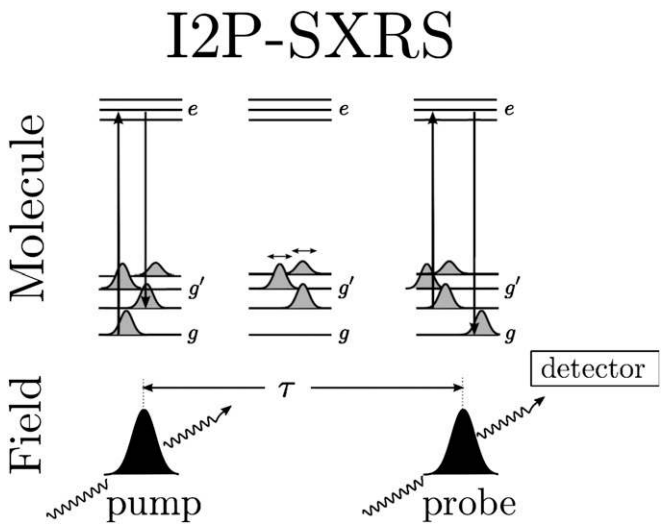

Fig. 1. The sequence of events underlying the SXRS signal. The molecule is initially in the ground electronic state g. The pump pulse creates a valence excitation g' through transient occupation of a core-excited state e. After a variable delay time τ, the probe pulse returns the system to the ground state via another core excitation. The signal is given by the change in the transmitted intensity of the probe due to the presence of the pump.

excited states after interaction with the first X-ray pulse. The second pulse interacts with this wavepacket via a second Raman process, and the change in its transmitted intensity is detected. We focus on the integrated two-pulse (I2P) SXRS signal defined as the change in the transmission of the second pulse with or without the pump pulse, recorded as a function of the time delay between the two pulses (Fig. 1). Because the core to valence transition frequency is element specific, this technique can be spatially selective. The signal is averaged over the isotropic distribution of molecular orientations. The probe polarization is set at the magic angle ($\theta = 54.7°$) with respect to the pump polarization, which allows the effective polarizability to be treated as a scalar rather than a tensor (31).

In addition to valence excitations, nuclear motions are also excited impulsively by the X-ray Raman process and should be taken into account for delays longer than the vibrational period (>5 fs). They are expected to add a vibronic fine structure to the valence electronic transitions that feature in the SXRS signals calculated here. Incorporating vibrational motions in superpositions of electronic states is an open computational challenge (42).

The I2P-SXRS signal is collected in the time domain, and a Fourier transform reveals the excitation frequencies of the valence-excited states that contribute. Expressions for the time- and frequency-domain I2P-SXRS signal are given in Eqs. **S1** and **S3** in *SI Text*, respectively. The signal is given by the imaginary part of the overlap $S_{\mathrm{I2P-SXRS}} = -\Im\langle\psi_W|\psi_D(\tau)\rangle$ between a time-dependent doorway state created by the first pulse and a window state created by the second pulse. When the pump pulse is tuned to the core edge of a selected atom, the valence wavepacket created by Raman interaction will initially be localized near that atom. In a porphyrin dimer two-color I2P-SXRS can directly monitor EET by tuning the pump and probe to be resonant with atoms located on different monomers. The signal vanishes for short delays and the time required to achieve the first maximum gives the EET coupling between monomers. The magnitude of the EET process is proportional to the spatial overlap between doorway and window states prepared on different monomers.

The feasibility of stimulated X-ray Raman in molecules using XFEL radiation has been examined by Patterson (43) and was demonstrated by recent pump–probe experiments in atoms (44, 45).

Results and Discussion

The chemical structure of the porphyrin dimer and the simulated X-ray absorption near-edge structure (XANES) for the nickel and the zinc $L_{2,3}$ -edge are shown in Fig. 2, together with the power spectra for the pulses used in our simulations. The zinc porphyrin ring is almost planar, whereas the nickel ring is distorted. In *SI Text* we show the calculated UV absorption spectrum and the XANES for the nickel and zinc K-edges in Figs. S1 and S2, respectively.

Note that the Raman process involves both photon absorption and emission. In a single-particle picture, a core electron is excited into a virtual orbital after which an electron from a valence orbital falls down and fills the core hole. The pulse bandwidth must encompass both the absorption and the emission frequencies. The XANES spectra in Fig. 2 reveal the pulse frequencies that contribute to the absorption, with the pulse center set to the core–edge transition. To see which frequencies contribute to the emission, it is necessary to collect the frequency-dispersed SXRS signal (47).

The I2P-SXRS signals in the time and frequency domain for the case where the pump is resonant with the zinc L-edge and the probe is resonant with either the zinc (Zn2p/Zn2p) or the nickel L-edge (Zn2p/Ni2p) are shown in Fig. 3. By tuning the pump and probe to either the K- or L- edge of nickel or zinc, there are sixteen different possible SXRS signals, which are depicted in Figs. S3–S5. Note from Fig. 2 that the amplitudes of the nickel 2p dipoles are larger than those for zinc, making the Zn2p/Zn2p signal weaker than the Zn2p/Ni2p signal. Peaks in the Fourier transform spectra correspond to electronic eigenstates of the dimer. In Fig. 3, *Right*, peaks labeled A, B, C, and C′ contribute to both signals, whereas peaks D, E, and F are visible only in the two-color signal.

The one-color Zn2p/Zn2p I2P-SXRS signal is maximal at $\tau = 0$, as the valence wavepacket is created and probed on the same atom. As τ grows, the excitation may spread throughout the molecule and onto the neighboring monomer, leading to a decrease in the signal amplitude. The signal shows strong beating, with a period of ~25 fs that equals the inverse frequency difference between the two dominant peaks at in the frequency domain, located at $\Omega =$ 4.74 eV (peak B in Fig. 3, *Right*) and 4.89 eV (peak C in Fig. 3, *Right*). Because these two peaks have the same sign in the frequency domain, this oscillation starts on a maximum rather than a minimum. [When two peaks in the frequency domain have the

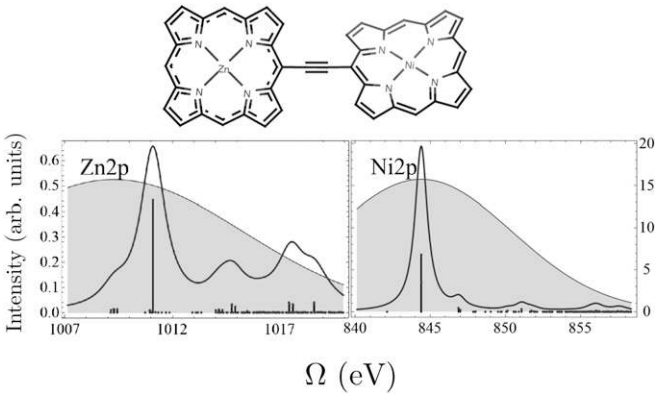

Fig. 2. (*Upper*) Chemical structure of the porphyrin heterodimer. (*Lower*) Simulated XANES for zinc and nickel $L_{2,3}$ -edge. All transitions have the same line width, 0.7 eV and 0.5 eV, respectively, taken from the ref. 46. Shaded areas show the power spectra of the transform-limited pulses used in our simulations with FWHM of 166 as (10.9 eV).

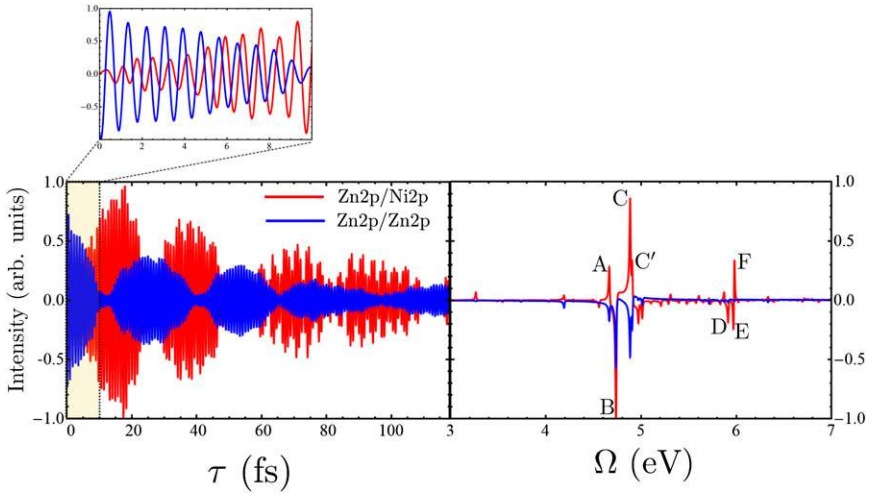

Fig. 3. (*Left*) The time-resolved I2P-SXRS signals for the porphyrin dimer for $0 \le \tau \le 120$ fs (given by Eq. S1). Shown are single-color Zn2p/Zn2p signal (in blue) and two-color Zn2p/Ni2p signal, with a zinc pump and nickel probe (in red). *Inset* shows the first 10 fs of the signals (*Left*, shaded region) on an expanded scale. (*Right*) Fourier transform of the *Left* (given by Eq. S2).

same (opposite) sign, the time-domain signal is proportional to the cosine (sine) of the frequency difference.] The signal is high initially, reaches a minimum near $\tau \simeq 12.2$ fs, and peaks again at $\tau \simeq 25$ fs.

The Zn2p/Ni2p signal starts at zero and grows to a maximum near 16 fs, a minimum at 28 fs, and another maximum near 38 fs. The maxima in the Zn2p/Ni2p signal roughly match with the minima in the Zn2p/Zn2p signal at the early time. However, there are many more spectral components and the time-domain signal is correspondingly richer at later times.

In *SI Text*, we also show the simulated frequency-dispersed two-pulse (D2P) SXRS signals in Figs. S6–S9. Experimentally, these are obtained by frequency resolving the probe pulse rather than recording its integrated intensity (47). These signals show the correlation between the valence-excited states that make up the I2P signal and the core-excited states off of which they scatter. The blue peaks in Fig. 3, *Right* are coupled to a Zn2p core-excited state with a frequency of 1,009.3 eV, which is not the dominant peak in the Zn2p XANES in Fig. 2. The red peaks are coupled to Ni2p core states with frequencies 844.4 eV and 846.9 eV, the latter of which is the dominant peak in the Ni2p XANES. In *SI Text* we show all of the 16 possible SXRS signals, where the pump and probe can be tuned to the K- or the L-edge of zinc or nickel, for reference.

Natural orbitals (NOs) (40) obtained through a singular-value decomposition of transition density matrices give a compact representation of single-particle valence excitations. When there is a single dominant NO transition (occupation number near 1), the excited state can be well described by an independent electron and hole. States with multiple NOs with nonnegligible occupation are

Table 1. Frequencies, participation ratios, and integrated electron and hole densities for the states corresponding to the major peaks in Fig. 3, *Right*

			Hole density		Electron density	
Peak	Ω	R^{-1}	Ni monomer	Zn monomer	Ni monomer	Zn monomer
A	4.67	1.57	0.41	0.59	0.38	0.62
B	4.74	2.45	0.37	0.63	0.29	0.71
C	4.89	4.48	0.34	0.66	0.40	0.60
C′	4.91	3.42	0.57	0.43	0.46	0.54
D	5.91	4.51	0.45	0.55	0.44	0.56
E	5.97	1.39	0.92	0.08	0.99	0.01
F	5.98	3.82	0.60	0.40	0.84	0.16

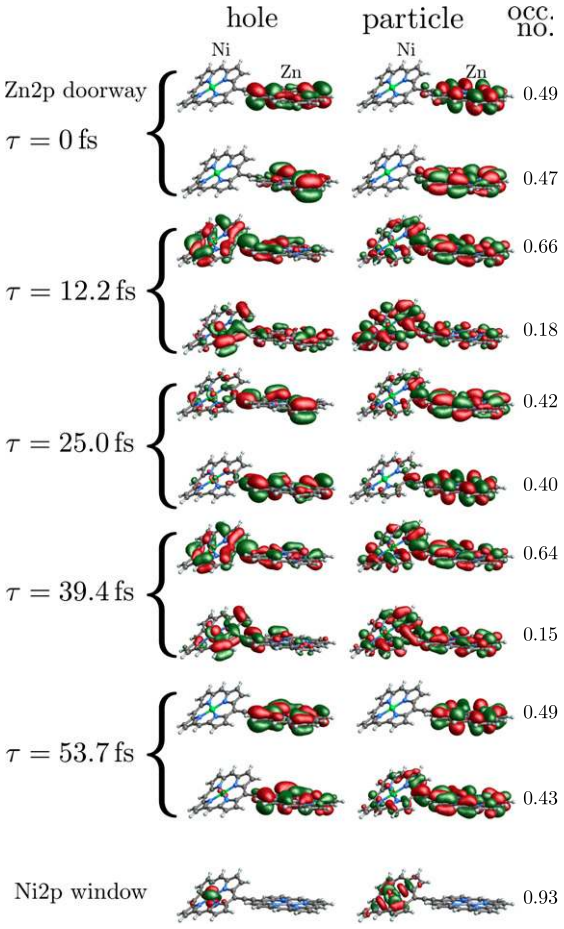

Fig. 4. (*Upper*) Dominant natural orbitals (NOs) for the Zn2p doorway wavepacket at different times. (*Lower*) NOs for the Ni2p window. *Left*, nickel monomer; *Right*, zinc monomer.

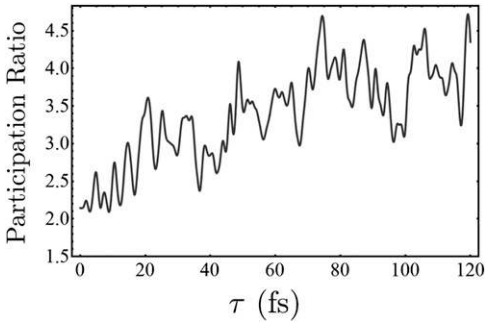

Fig. 5. Participation ratio for the time-dependent Zn2p doorway wavepacket. A value of 1 indicates the electron and hole are uncorrelated, and a higher value indicates the greater degree of entanglement between different electron–hole pairs.

inherently multiconfigurational in nature, and the electron and hole are entangled. A useful measure of this entanglement (41) is the participation ratio (PR) R^{-1}, where R is the sum of the squared occupation numbers for all NO pairs (Eq. **S22** in *SI Text*). The PR varies between 1 (no entanglement, uncorrelated electron and hole) and the number of possible excitations. The PRs for the peaks in Fig. 3 are given in Table 1. Fig. S10 shows the NOs for the valence-excited states corresponding to the peaks in Fig. 3. Only the valence state corresponding to peak E is well represented by a single NO electron-hole pair, with an occupation number of 0.85. As we see from the integrated densities in Table 1, peak E is also the only valence eigenstate which is largely localized to a single monomer.

The natural orbital decomposition was used to visualize the superposition of the excited states created by the Raman excitation (see *SI Text* for detailed expressions). We show the dominant NO for the real-valued Ni2p window wavepacket in Fig. 4, *Lower*. Both electron and hole are entirely localized to the nickel monomer, with the hole more tightly focused near the nickel atom and with a participation ratio of 1.15, unentangled. The doorway state is time dependent and complex valued, but the signal is proportional to its imaginary part. In Fig. 4, *Upper* we plot NOs for the imaginary part of the Zn2p doorway for five time points, corresponding to peaks and troughs in the Zn2p/Zn2p signal. At all times, the doorway is multiconfigurational in nature, as can be seen in the time-dependent PR shown in Fig. 5; we show only the two with the highest occupation numbers. Initially, the doorway resides entirely on the zinc monomer. At times $\tau = 12.2$ fs and $\tau = 39.4$ fs, it has delocalized over the whole dimer. At times $\tau = 25.0$ fs and $\tau = 53.7$ fs, the doorway has relocalized on the zinc monomer.

In Fig. S11, we give the time-dependent participation ratio for doorway wavepackets created at the K- and L-edges of zinc and nickel. The Zn2p wavepacket is unique in having a large PR, which starts at a value of $\sim$ 2 and grows as high as 4.5 in the first 120 fs after excitation. The PR for Zn1s excitation stays below 2 for all times, and the Ni1s and Ni2p PRs stay below 1.5. Interestingly, it is only the Zn2p wavepacket that exhibits strong EET. This can be seen by comparing the Zn2p/Zn2p I2P-SXRS signal, which shows strong low-frequency oscillations, with the other three one-color signals that exhibit only exponential decay. These results suggest a correlation between a high PR and efficient EET. The theoretical basis for this observation is not obvious.

To further visualize the excited state dynamics, we examine the time-dependent electron and hole densities, integrated over spatial regions containing either the zinc or the nickel monomers, using the method described in *SI Text*. A perpendicular plane through the center of the carbon triple bond was used to separate the zinc and nickel monomer regions. In Fig. 6 we show the integrated densities for the zinc doorway, as well as the densities for various time points. Movie S1 shows the electron and hole densities for the first 120 fs following Zn2p excitation. We can see clearly from Fig. 6, *Left* and *Right* that the electron and hole densities change in the same phase. Each ring remains neutral; this is energy, not charge, transfer.

Conclusions

The I2P-SXRS technique is ideally suited for creating localized excitations in molecules and monitoring the ensuing dynamics with attosecond time resolution, taking advantage of the current- and next-generation XFEL sources. Here we have shown that the time-dependent signal reveals the back-and-forth energy transfer in this model system. Compared to optical pulses, X-ray pulses create more localized excitations, so that they can trigger and measure

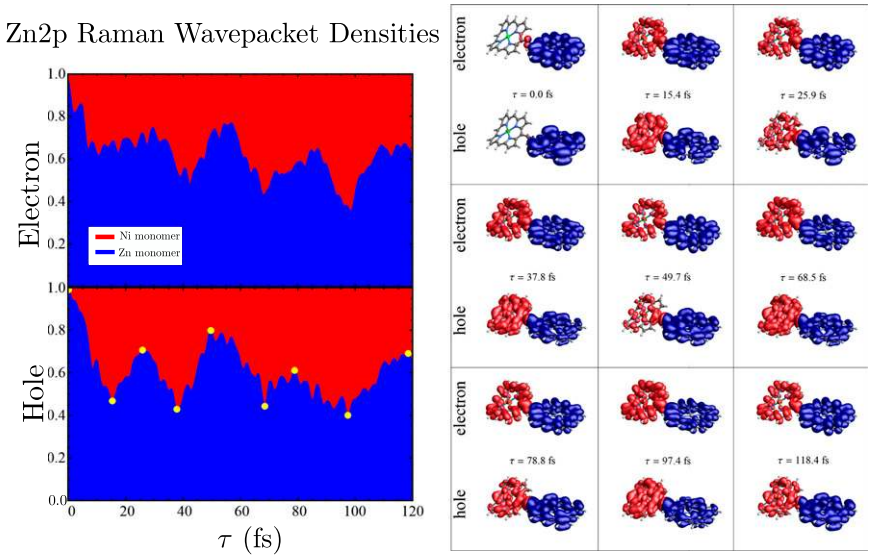

Fig. 6. (*Right*) Electron and hole densities for the Zn2p valence superposition state prepared by SXRS for various times after excitation. The isosurfaces are colored according to which monomer they reside on, red for nickel and blue for zinc. (*Left*) Spatially integrated densities over each ring. (*Lower Left*) The yellow dots correspond to the time points for which snapshots are shown on the *Right*. Movie S1 shows the electron and hole motion.

excited state dynamics at specific positions in a molecular system. In addition, the X-ray Raman technique, thanks to the large bandwidth of attosecond pulses, can populate high-energy valence-excited states that may not be accessible from the ground state by visible pulses. Both of these features make stimulated X-ray Raman spectroscopy a powerful tool to observe EET in complex molecular systems.

Materials and Methods

Computational Details. A restricted excitation window time-dependent density functional theory (REW-TDDFT) formalism was recently extended to treat X-ray core excitations, using a realistic treatment of valence electron correlation (48), which scales well to larger systems. The ground-state geometry of a Zn/Ni porphyrin heterodimer (Fig. 2) was optimized using Gaussian09 (49) at the B3LYP (50, 51)/6-31G* level of theory. Transition dipoles and core excitation frequencies were calculated using REW-TDDFT (48, 52–54). We adopt the computational protocol in ref. 55. All REW-TDDFT calculations were performed with a locally modified version of NWChem code (56) at the CAM-B3LYP (57)/6-311G** level of theory and within the Tamm–Dancoff approximation (58). We assume transform-limited Gaussian pulses in our simulations with FWHM of 166 as (10.9 eV). The pulse power spectra are shown as shaded areas along with the XANES in Fig. 2.

ACKNOWLEDGMENTS. Help on the REW-TDDFT calculations from Niranjan Govind of the Pacific Northwest National Laboratory is greatly appreciated. We gratefully acknowledge support from the Chemical Sciences, Geosciences, and Biosciences Division, Office of Basic Energy Sciences, Office of Science, US Department of Energy, as well as from the National Science Foundation (Grant CHE-1058791) and the National Institutes of Health (Grant GM-59230).

1. Nakamura Y, Aratani N, Osuka A (2007) Cyclic porphyrin arrays as artificial photosynthetic antenna: Synthesis and excitation energy transfer. *Chem Soc Rev* 36(6): 831–845.
2. Yang J, Yoon MC, Yoo H, Kim P, Kim D (2012) Excitation energy transfer in multiporphyrin arrays with cyclic architectures: Towards artificial light-harvesting antenna complexes. *Chem Soc Rev* 41(14):4808–4826.
3. Panda MK, Ladomenou K, Coutsolelos AG (2012) Porphyrins in bio-inspired transformations: Light-harvesting to solar cell. *Coord Chem Rev* 256(21-22):2601–2627.
4. Li LL, Diau EWG (2013) Porphyrin-sensitized solar cells. *Chem Soc Rev* 42(1):291–304.
5. Shirsat MD, et al. (2012) Porphyrin-functionalized single-walled carbon nanotube chemiresistive sensor arrays for vocs. *J Phys Chem C* 116(5):3845–3850.
6. Ethirajan M, Chen Y, Joshi P, Pandey RK (2011) The role of porphyrin chemistry in tumor imaging and photodynamic therapy. *Chem Soc Rev* 40(1):340–362.
7. Ishizuka T, et al. (2011) The roles of molecular structure and effective optical symmetry in evolving dipolar chromophoric building blocks to potent octopolar nonlinear optical chromophores. *J Am Chem Soc* 133(9):2884–2896.
8. Jiang N, et al. (2012) Design of coupled porphyrin chromophores with unusually large hyperpolarizabilities. *J Phys Chem C* 116(17):9724–9733.
9. Senge MO, et al. (2007) Nonlinear optical properties of porphyrins. *Adv Mater* 19(19): 2737–2774.
10. Jurow M, Schuckman AE, Batteas JD, Drain CM (2010) Porphyrins as molecular electronic components of functional devices. *Coord Chem Rev* 254(19–20):2297–2310.
11. Lindsey JS, Bocian DF (2011) Molecules for charge-based information storage. *Acc Chem Res* 44(8):638–650.
12. Hasobe T (2012) Photo- and electro-functional self-assembled architectures of porphyrins. *Phys Chem Chem Phys* 14(46):15975–15987.
13. Cho WJ, Cho Y, Min SK, Kim WY, Kim KS (2011) Chromium porphyrin arrays as spintronic devices. *J Am Chem Soc* 133(24):9364–9369.
14. Ma Y, Dai Y, Zhang Z, Yu L, Huang B (2012) Magnetic properties of phthalocyanine-based organometallic nanowire. *Appl Phys Lett* 101(6):062405-(1-4).
15. Kepenekian M, et al. (2011) Toward reliable dft investigations of mn-porphyrins through caspt2/dft comparison. *J Chem Theory Comput* 7(11):3532–3539.
16. Locos O, Bašić B, McMurtrie JC, Jensen P, Arnold DP (2012) Homo- and heteronuclear meso,meso-(E)-ethene-1,2-diyl-linked diporphyrins: Preparation, x-ray crystal structure, electronic absorption and emission spectra and density functional theory calculations. *Chemistry* 18(18):5574–5588.
17. Cho S, Yoon MC, Kim KS, Kim P, Kim D (2011) Electron delocalization in various triply linked zinc(II) porphyrin arrays: Role of antiaromatic junctions between aromatic porphyrins. *Phys Chem Chem Phys* 13(36):16175–16181.
18. Kumar D, et al. (2009) Effect of porphyrin ligands on the regioselective dehydrogenation versus epoxidation of olefins by oxoiron(IV) mimics of cytochrome P450. *J Phys Chem A* 113(43):11713–11722.
19. Chen H, Lai W, Shaik S (2011) Multireference and multiconfiguration ab initio methods in heme-related systems: What have we learned so far? *J Phys Chem B* 115(8):1727–1742.
20. Ghosh A (1998) First-principles quantum chemical studies of porphyrins. *Acc Chem Res* 31(4):189–198.
21. Baerends E, Ricciardi G, Rosa A, van Gisbergen S (2002) A dft/tddft interpretation of the ground and excited states of porphyrin and porphyrazine complexes. *Coord Chem Rev* 230(1-2):5–27.
22. Gao G, Kang HS (2010) Engineering of the electronic structures of metal-porphyrin tapes and metal-hexaphyrin tapes: A first-principles study. *Chem Phys* 369(2-3):66–70.
23. Li LH, Li JQ, Wu LM (2012) Polymeric fused-ring type iron phthalocyanine nanosheet and its derivative ribbons and tubes. *J Phys Chem C* 116(16):9235–9242.
24. Kim D, ed (2012) *Multiporphyrin Arrays: Fundamentals and Applications* (Pan Stanford, Singapore).
25. Cho HS, et al. (2003) Excitation energy transport processes of porphyrin monomer, dimer, cyclic trimer, and hexamer probed by ultrafast fluorescence anisotropy decay. *J Am Chem Soc* 125(19):5849–5860.
26. Kumble R, Palese S, Lin VSY, Therien MJ, Hochstrasser RM (1998) Ultrafast dynamics of highly conjugated porphyrin arrays. *J Am Chem Soc* 120(44):11489–11498.
27. Emma P, et al. (2010) First lasing and operation of an angstrom-wavelength free-electron laser. *Nat Photonics* 4(9):641–647.
28. Ullrich J, Rudenko A, Moshammer R (2012) Free-electron lasers: New avenues in molecular physics and photochemistry. *Annu Rev Phys Chem* 63:635–660.
29. Popmintchev T, Chen M, Arpin P, Murnane MM, Kapteyn HC (2010) The attosecond nonlinear optics of bright coherent X-ray generation. *Nat Photonics* 4(12):822–832.
30. Gallmann L, Cirelli C, Keller U (2012) Attosecond science: Recent highlights and future trends. *Annu Rev Phys Chem* 63:447–469.
31. Mukamel S, Healion D, Zhang Y, Biggs JD (2013) Multidimensional attosecond resonant X-ray spectroscopy of molecules: Lessons from the optical regime. *Annu Rev Phys Chem* 64:101–127.
32. Lutman AA, et al. (2013) Experimental demonstration of femtosecond two-color x-ray free-electron lasers. *Phys Rev Lett* 110(13):134801-(1-5).
33. Kern J, et al. (2013) Simultaneous femtosecond X-ray spectroscopy and diffraction of photosystem II at room temperature. *Science* 340(6131):491–495.
34. Schiffrin A, et al. (2013) Optical-field-induced current in dielectrics. *Nature* 493(7430): 70–74.
35. Lemke HT, et al. (2013) Femtosecond X-ray absorption spectroscopy at a hard X-ray free electron laser: Application to spin crossover dynamics. *J Phys Chem A* 117(4):735–740.
36. Dell'Angela M, et al. (2013) Real-time observation of surface bond breaking with an x-ray laser. *Science* 339(6125):1302–1305.
37. Goulielmakis E, et al. (2010) Real-time observation of valence electron motion. *Nature* 466(7307):739–743.
38. Wirth A, et al. (2011) Synthesized light transients. *Science* 334(6053):195–200.
39. Glownia JM, et al. (2010) Time-resolved pump-probe experiments at the LCLS. *Opt Express* 18(17):17620–17630.
40. Martin RL (2003) Natural transition orbitals. *J Chem Phys* 118(11):4775–4777.
41. Mukamel S, Wang H (2010) Manipulating quantum entanglement of quasiparticles in many-electron systems by attosecond X-ray pulses. *Phys Rev A* 81(6):062334-(1-4).
42. Nikoobakht B, Köppel H, Gindensperger E, Cederbaum LS (2012) Efficient computation of adiabatic electronic populations in multi-mode vibronic systems: Theory, implementation, and application. *J Chem Phys* 137(11):114110-(1-14).
43. Patterson B (2010) Resource letter on stimulated inelastic X-ray scattering at an XFEL. Technical report (SLAC National Accelerator Laboratory, Menlo Park, CA). Available at http://slac.stanford.edu/pubs/slactns/tn04/slac-tn-10-026.pdf. Accessed August 18, 2013.
44. Doumy G, et al. (2011) Nonlinear atomic response to intense ultrashort x rays. *Phys Rev Lett* 106(8):083002-(1-4).
45. Young L, et al. (2010) Femtosecond electronic response of atoms to ultra-intense X-rays. *Nature* 466(7302):56–61.
46. Zschornack GH (2007) *Handbook of X-ray Data* (Springer, Berlin Heidelberg), 1st Ed.
47. Biggs JD, Zhang Y, Healion D, Mukamel S (2013) Multidimensional X-ray spectroscopy of valence and core excitations in cysteine. *J Chem Phys* 138(14):144303-(1-14).
48. Lopata K, Van Kuiken BE, Khalil M, Govind N (2012) Linear-response and real-time time-dependent density functional theory studies of core-level near-edge X-ray absorption. *J Chem Theory Comput* 8(9):3284–3292.
49. Frisch MJ, et al. (2009) *Gaussian 09, Revision c.01* (Gaussian, Wallingford, CT).
50. Becke AD (1993) Density-functional thermochemistry. III. The role of exact exchange. *J Chem Phys* 98(7):5648–5652.
51. Stephens PJ, Devlin FJ, Chabalowski CF, Frisch MJ (1994) Ab initio calculation of vibrational absorption and circular dichroism spectra using density functional force fields. *J Phys Chem* 98(45):11623–11627.
52. Stener M, Fronzoni G, de Simone M (2003) Time dependent density functional theory of core electrons excitations. *Chem Phys Lett* 373(1-2):115–123.
53. Besley NA, Noble A (2007) Time-dependent density functional theory study of the X-ray absorption spectroscopy of acetylene, ethylene, and benzene on si(100). *J Phys Chem C* 111(8):3333–3340.
54. DeBeer-George S, Petrenko T, Neese F (2008) Time-dependent density functional calculations of ligand k-edge X-ray absorption spectra. *Inorg Chim Acta* 361(4):965–972.
55. Zhang Y, Biggs JD, Healion D, Govind N, Mukamel S (2012) Core and valence excitations in resonant X-ray spectroscopy using restricted excitation window time-dependent density functional theory. *J Chem Phys* 137(19):194306-(1-10).
56. Valiev M, et al. (2010) NWChem: A comprehensive and scalable open-source solution for large scale molecular simulations. *Comput Phys Commun* 181(9):1477–1489.
57. Yanai T, Tew D, Handy N (2004) A new hybrid exchange correlation functional using the coulomb-attenuating method (CAM-B3LYP). *Chem Phys Lett* 393(1-3):51–57.
58. Hirata S, Head-Gordon M (1999) Time-dependent density functional theory within the Tamm-Dancoff approximation. *Chem Phys Lett* 314-(3-4):291–299.

Supporting Information

Biggs et al. 10.1073/pnas.1308604110

SI Text

Absorption Spectra

The absorption spectra in the UV and X-ray regions are shown in Figs. S1 and S2, respectively.

Expressions for Stimulated X-Ray Raman Spectroscopy Signals

$$S_{\mathrm{I2P}}(\tau) = 2\Im\left\langle \alpha_2''(\tau)\alpha_1(0)\right\rangle = 2\Im\sum_{g'} e^{-i\omega_{g'g}\tau-\Gamma_{g'}\tau}\alpha''_{2;g\,g'}\alpha_{1;g'g}, \quad \text{[S1]}$$

where

$$\alpha_j = \alpha_j' + i\alpha_j'' = \sum_{e,g'g''} |g'\rangle\frac{\mu_{g'e}\mu_{eg''}}{2\pi}\int_{-\infty}^{\infty} d\omega\,\frac{\mathcal{E}_j^*(\omega)\mathcal{E}_j(\omega+\omega_{g'g''})}{\omega-\omega_{eg'}+i\Gamma_e}\langle g''| \quad \text{[S2]}$$

is the effective isotropic polarizability of the molecule, averaged over the spectral envelope of the jth ultrashort pulse, $\mathcal{E}_j$. $\omega_{g'g}$ and $\Gamma_{g'}$ are the excitation frequency and the phenomenological line width for the $g\to g'$ transition. In lieu of a more sophisticated model for interaction with the environment (bath), we set $\Gamma g' = 0.006$ eV for all valence-excited states for convenience. This is consistent with the electronic lifetime ($\Gamma_{g'}^{-1} = 100$ fs) typical for valence excitations. Core lifetime broadening coefficients were taken from ref. 1 and are $\Gamma_{\mathrm{Zn1s}} = 1.67$ eV, $\Gamma_{\mathrm{Zn2p}} = 0.70$ eV, $\Gamma_{\mathrm{Ni1s}} = 1.44$ eV, and $\Gamma_{\mathrm{Ni2p}} = 0.50$ eV.

The summation in Eq. **S1** is over the set of valence-excited states g'. This formula contains only the valence-excited coherence and ignores any core-excited population created by the first X-ray pulse. The core edges considered here, the K- and L-edges of zinc and nickel, have lifetimes of a few femtoseconds (1), after which Auger processes are expected to fill the core hole and ionize the molecule, taking it out of resonance with the probe pulse. Therefore, the signals presented here are accurate only for longer times. The stimulated X-ray Raman spectroscopy (SXRS) signal is experimentally collected in the time domain, and a numerical Fourier transform reveals the excitation frequencies of the valence-excited states that contribute:

$$S_{\mathrm{I2P}}(\Omega) = -\sum_{g'}\left(\frac{\alpha''_{2;gg'}\alpha_{1;g'g}}{\Omega_2-\omega_{g'g}+i\Gamma_{g'}} + \frac{(\alpha''_{2;gg'}\alpha_{1;g'g})^*}{\Omega_2+\omega_{g'g}+i\Gamma_{g'}}\right). \quad \text{[S3]}$$

The calculation of the effective polarizability requires the transition dipoles and energy differences between the set of valence states $|g'\rangle$ and the set of core-excited states $|e\rangle$. In Eq. **S2**, we see that those core-excited states whose excitation energies are within the pulse bandwidth will dominate the Raman process.

A 2D dispersed two-pulse (D2P)-SXRS signal is obtained by sending the probe through a spectrometer and recording the dispersed spectrum vs. the interpulse delay,

$$S_{\text{D2P-SXRS}}(t_2,\Omega_3) = \Im\mathcal{E}_2^*(\Omega_3)P^{(3)}(t_2,\Omega_3). \quad \text{[S4]}$$

A Fourier transform with respect to the delay time yields

$$S_{\text{D2P-SXRS}}(\Omega_2,\Omega_3) = \sum_{e,g'}\frac{iV_{ge}V_{eg'}(\alpha_{1;g'g})}{\Omega_2-\omega_{g'g}+i\Gamma_{g'}} \times\left(\frac{\mathcal{E}_2(\Omega_3+\omega_{gg'})\mathcal{E}_2^*(\Omega_3)}{\Omega_3-\omega_{eg}+i\Gamma_e} - \frac{\mathcal{E}_2^*(\Omega_3+\omega_{g'g})\mathcal{E}_2(\Omega_3)}{\Omega_3-\omega_{eg'}-i\Gamma_e}\right). \quad \text{[S5]}$$

SXRS Spectra

Figs. S3–S5 depict all 16 possible integrated two-pulse (I2P)-SXRS signals for the porphyrin dimer, in both the time and the frequency domains. The signals are labeled with the pulses listed from left to right, so that the Zn1s/Ni1s signal has the pump and probe tuned to the zinc and nickel K-edges, respectively. The signals have each been normalized before plotting.

There are four single-color I2P-SXRS signals shown in Fig. S4. In a single-color experiment, the doorway and window wavepackets are initially nearly identical. The Ni1s/Ni1s signal starts off large and decays exponentially. On top of this exponential decay is a high-frequency oscillation corresponding to the only significant peak in the Fourier transform spectrum, labeled herein as S_{98}, the 98th excited singlet state, at $\Omega = 6.13$ eV. A similar tale is told by the Zn1s/Zn1s signal. Here again there is a single dominant contribution, state S_{63} with a frequency of 5.48 eV.

The following two single-color I2P-SXRS signals use 2p orbitals for the core hole. The Ni2p/Ni2p spectrum features two strong peaks at $\Omega = 2.02$ eV and 2.58 eV, respectively (the first peak is actually two peaks, at 2.018 eV and 2.023 eV, which are unresolvable using the line width in this simulation). In the time domain this manifests as high-frequency oscillation, with a period matching the inverse frequency of the valence-excited states, on top of a lower-frequency oscillation corresponding to beat frequencies between the different Fourier components. The final single-color SXRS signal, Zn2p/Zn2p, in the main text is qualitatively different from the others.

The two-color I2P-SXRS signals come in two varieties: those that probe the same atom at different shells, such as the Ni2p/Ni1s signal, and those that probe different atoms, such as the Zn1s/Ni1s signal. The Ni1s/Ni2p signal shown in Fig. S5 has one dominant spectral component at $\Omega = 6.13$ eV, with smaller peaks at 4.03 eV and 7.08 eV. The time-domain signal is similar to the Ni1s/Ni1s signal; indeed, the dominant peak is in both spectra. The Ni2p/Ni1s signal in Fig. S6 is nearly identical to the Ni1s/Ni2p signal (they are taken with the same experimental setup, changing the delay time from positive to negative). Any difference between the two is related to the difference between α, which contains resonant and off-resonant contributions, and α'', which vanishes when the pulse is detuned off resonance. The corresponding zinc signals, Zn1s/Zn2p and Zn2p/Zn1s, have many different spectral components, and the overlap between doorway and window shows a complicated beating pattern.

It is the latter category of two-color I2P-SXRS signals, where the doorway and window wavepackets are created at different metal centers located on different porphyrin subunits, that most directly reports on excitation energy transfer (EET). The observable in an I2P-SXRS experiment is defined as the difference in probe transmission due to the presence of the pump and therefore would be zero if the monomers were uncoupled. The fact that the doorway and window wavepacket have nonzero overlap indicates that the valence systems of both monomers do indeed interact.

There are eight such signals, but given the near symmetry between signals taken with the pump and probe reversed, we can focus on only four: Ni1s/Zn1s, Ni1s/Zn2p, Ni2p/Zn1s, and Ni2p/Zn2p (all shown in Fig. S5). The Ni1s/Zn1s signal, which in the time domain starts at zero and grows in over the first 5 fs before decreasing again, is especially suggestive of back-and-forth excitation transfer between monomers. The roughly 10-fs period present in this signal matches the beat frequency between peaks at 6.56 eV and 6.13 eV, and the fact that the signal starts at zero is due to the fact that these peaks have opposite sign in the frequency domain.

Interestingly, the Zn2p/Ni1s and Zn1s/Ni2p signals are much more complex than the Zn1s/Ni1s and Zn2p/Ni2p signals. All four signals have in common that they start from zero and grow initially, but the Zn2p/Ni1s and Zn1s/Ni2p signals do not show strong coherent low-frequency motion.

Figs. S6–S9 show the D2P-SXRS signals, obtained by frequency dispersing the probe pulse. The one-dimensional I2P-SXRS signal is found by integrating the 2D D2P-SXRS signal. These signals show the coupling between core and valence excitations directly, allowing us to probe inside the effective polarizability. We see that the core states that dominate the X-ray absorption spectra (XANES) are not necessarily the most important for the SXRS signal. The former depend only on the dipole between the ground and the core states, whereas the latter depend also on the dipole between core and valence-excited states. Fig. S10 shows the largest-amplitude NTOs for the valence-excited eigenstates corresponding to the dominant peaks in Fig. 3 of the main text.

Natural Orbital Decomposition

Interaction with the pump creates the doorway

$$\left|\psi_D(\tau)\right\rangle = \sum_{g'} \alpha_{1;g'g_o} e^{-i\epsilon_{g'}\tau} \left|g'\right\rangle. \quad \text{[S6]}$$

This is a wavepacket of valence-excited states, each of which can be represented as a linear combination of particle–hole excitations

$$\left|g'\right\rangle = \sum_{ai} C_{ai}^{g'} c_a^\dagger c_i \left|g\right\rangle, \quad \text{[S7]}$$

where $c_a^\dagger$ (c_i) is the creation (annihilation) operator for the virtual (occupied) orbital a (i). We define the time-dependent transformation operator between the occupied and unoccupied orbital spaces,

$$\hat{K}(\tau) = \sum_{g,ai} \alpha_{1;g'g_o} C_{ai}^{g'} c_a^\dagger c_i e^{-i\epsilon_{g'}\tau}. \quad \text{[S8]}$$

The doorway can be obtained by acting with this operator on the ground state

$$\left|\psi_D(\tau)\right\rangle = \hat{K}(\tau)\left|g\right\rangle. \quad \text{[S9]}$$

The singular value decomposition (SVD) of $\hat{K}(\tau)$ provides a compact particle–hole representation of the doorway state in the space of single excitations (2),

$$K(\tau) = V(\tau)W(\tau)U^\dagger(\tau). \quad \text{[S10]}$$

The matrices $V(\tau)$ and $U(\tau)$ are unitary, and $W(\tau)$ is a diagonal matrix with real, nonnegative elements $w_\xi(\tau)$.

SVD allows to recast the doorway as

$$\left|\psi_D(\tau)\right\rangle = \sum_{\xi} w_\xi(\tau) c_\xi^\dagger(\tau) d_\xi(\tau) \left|g\right\rangle, \quad \text{[S11]}$$

where

$$c_\xi^\dagger(\tau) = \sum_a V_{a,\xi}(\tau) c_a^\dagger \quad \text{[S12]}$$

and

$$d_\xi(\tau) = \sum_i U_{i,\xi}^*(\tau) c_i \quad \text{[S13]}$$

are the creation and annihilation operators for the natural particle–hole orbitals, respectively. Because the doorway is normalized before application of the SVD, we have at all times

$$\sum_\xi w_\xi^2(\tau) = 1. \quad \text{[S14]}$$

The participation ratio, a useful measure of the degree to which the electron and the hole are entangled, is given by

$$R^{-1}(\tau) = \frac{1}{\sum_\xi w_\xi^4(\tau)}. \quad \text{[S15]}$$

In Fig. S11 we show the participation ratio for wavepackets at the K- and L-edges for zinc and nickel. We can see that Zn2p is unique in having a highly entangled electron and hole.

The Reduced Particle–Hole Densities

We define a density matrix corresponding to our pure state

$$\hat{\rho}(\tau) = \left|\psi(\tau)\right\rangle\left\langle\psi(\tau)\right|. \quad \text{[S16]}$$

This allows us to define the reduced particle density matrix

$$\begin{aligned} \sigma_p &= \mathrm{Tr}_h\left[\hat{\rho}(\tau)\right] \\ &= K(\tau)K^\dagger(\tau) \\ (\sigma_p)_{ba} &= \sum_\xi w_\xi^2 V_{\xi,a}^* V_{\xi,b}. \end{aligned} \quad \text{[S17]}$$

Similarly, we have for the hole

$$\begin{aligned} \sigma_h &= \mathrm{Tr}_e\left[\hat{\rho}(\tau)\right] \\ &= K^\dagger(\tau)K(\tau) \\ (\sigma_h)_{ij} &= \sum_\xi w_\xi^2 U_{\xi,i} U_{\xi,j}^*. \end{aligned} \quad \text{[S18]}$$

In real space we can write

$$\sigma_h(\mathbf{r}',\mathbf{r}) = \sum_{\xi,ij} \phi_j^*(\mathbf{r}') U_{\xi,j}^* w_\xi^2 U_{\xi,i} \phi_i(\mathbf{r}) \quad \text{[S19]}$$

and

$$\sigma_p(\mathbf{r}',\mathbf{r}) = \sum_{\xi,ab} \phi_b(\mathbf{r}') V_{\xi,b} w_\xi^2 V_{\xi,a}^* \phi_a^*(\mathbf{r}). \quad \text{[S20]}$$

The diagonal parts of these operators

$$\sigma_{h,p}(\mathbf{r}) = \int \sigma_{h,p}(\mathbf{r}',\mathbf{r}) \delta(\mathbf{r}-\mathbf{r}') \mathrm{d}\mathbf{r}' \quad \text{[S21]}$$

describe the spatial probability for finding the electron or the hole at a given point in space. Eq. **S21** is used to construct the density plots in Fig. 6 of the main text. The off-diagonal parts $\mathbf{r} \neq \mathbf{r}'$ represent spatial coherences.

1. Zschornack GH (2007) *Handbook of X-Ray Data* (Springer, Berlin Heidelberg), 1st Ed.

2. Martin RL (2003) Natural transition orbitals. *J Chem Phys* 118(11):4775–4777.

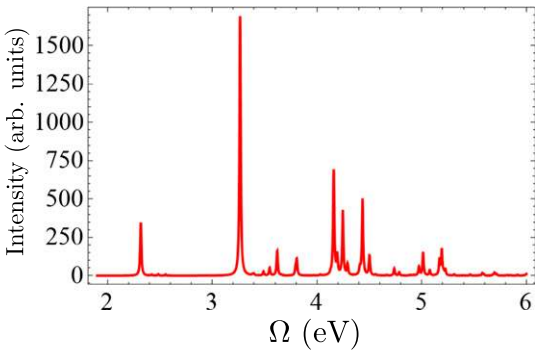

Fig. S1. UV absorption spectrum for the porphyrin dimer, using a uniform line width 0.006 eV.

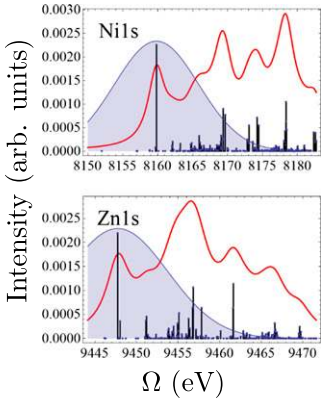

Fig. S2. Simulated K-edge XANES for zinc and nickel, using uniform line widths of 1.67 eV and 1.44 eV, respectively.

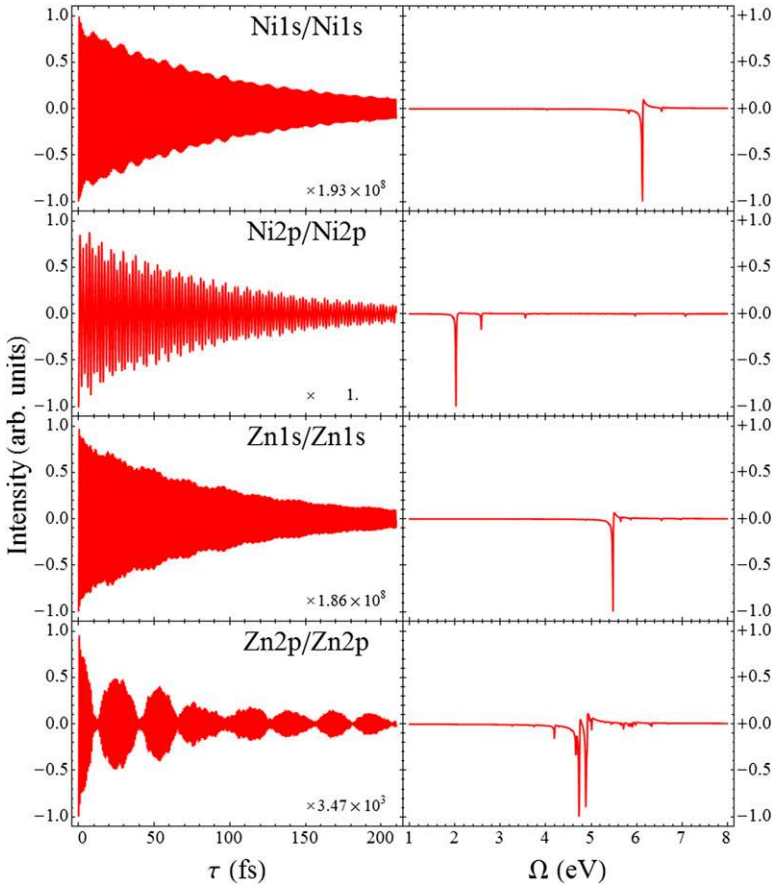

Fig. S3. Single-color I2P-SXRS signals from the porphyrin dimer.

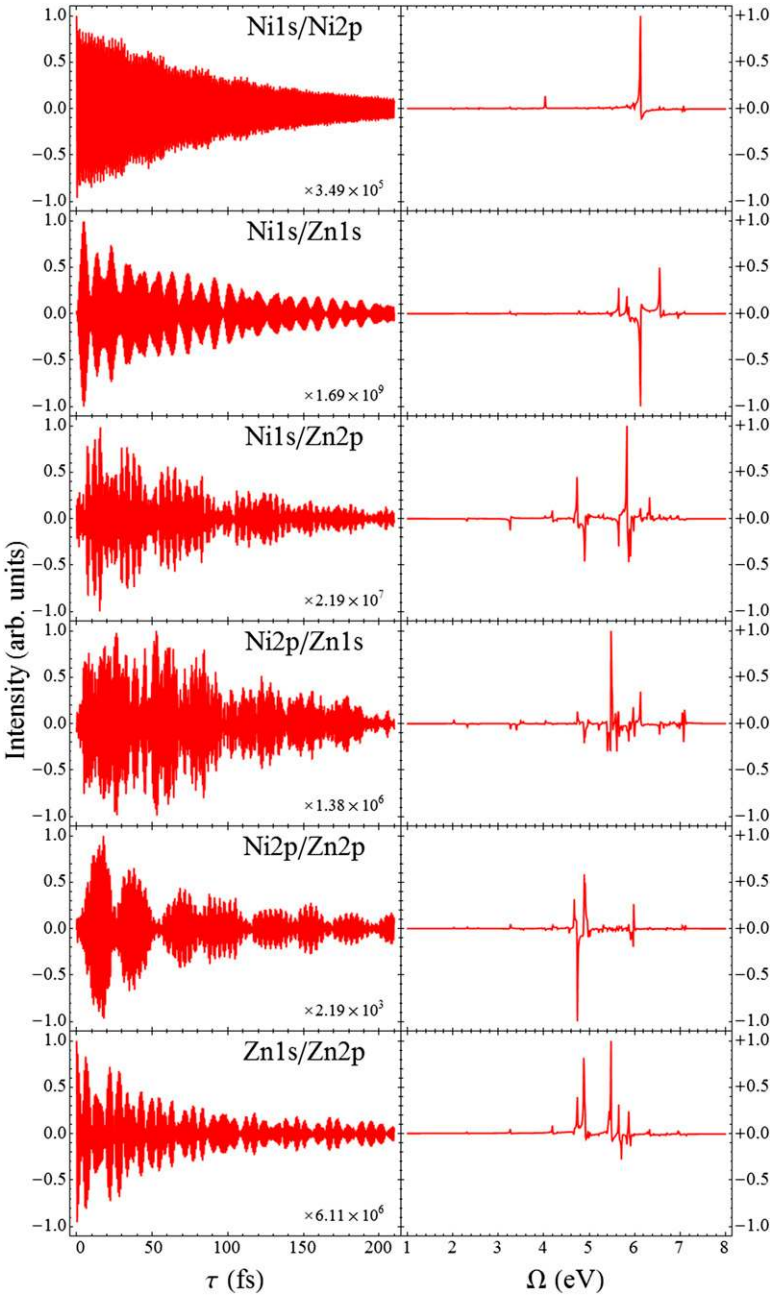

Fig. S4. Six of the two-color I2P-SXRS signals.

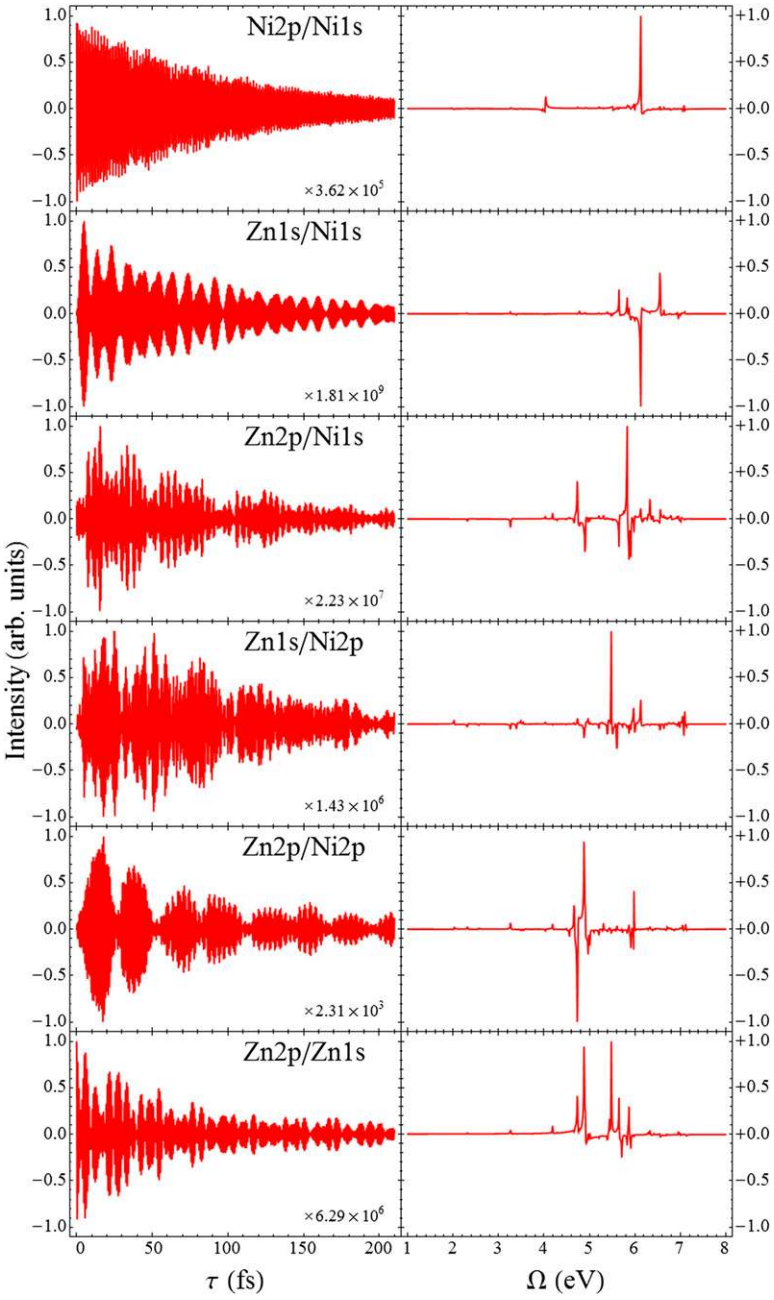

Fig. S5. The six two-color I2P-SXRS signals not shown in Fig. S4.

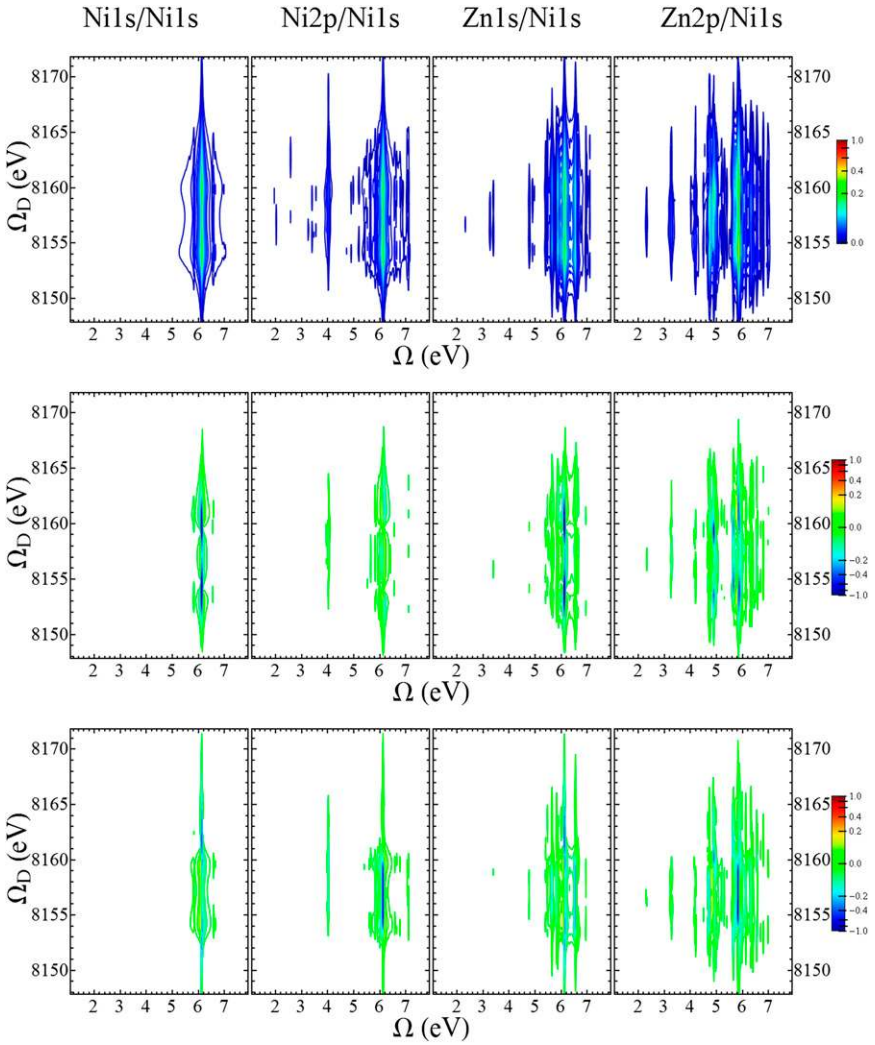

Fig. S6. Dispersed two-pulse Raman signal (Eq. **S5**), with the probe pulse at the nickel K-edge. The *x* axis is the Fourier conjugate of the delay time, and the *y* axis is the dispersed frequency. *Top*, *Middle*, and *Bottom* show the modulus, real, and imaginary parts of the signal, respectively.

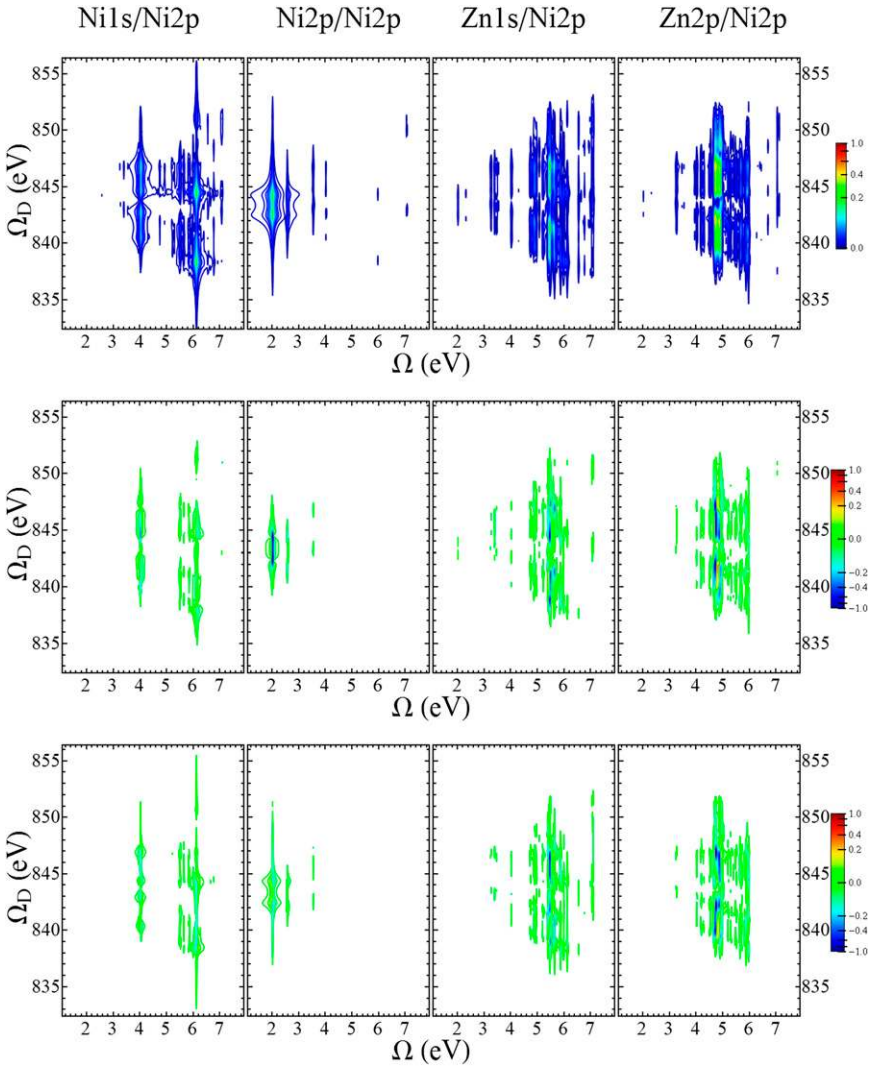

Fig. S7. The same as for Fig. S7 but with the probe tuned to the nickel L-edge.

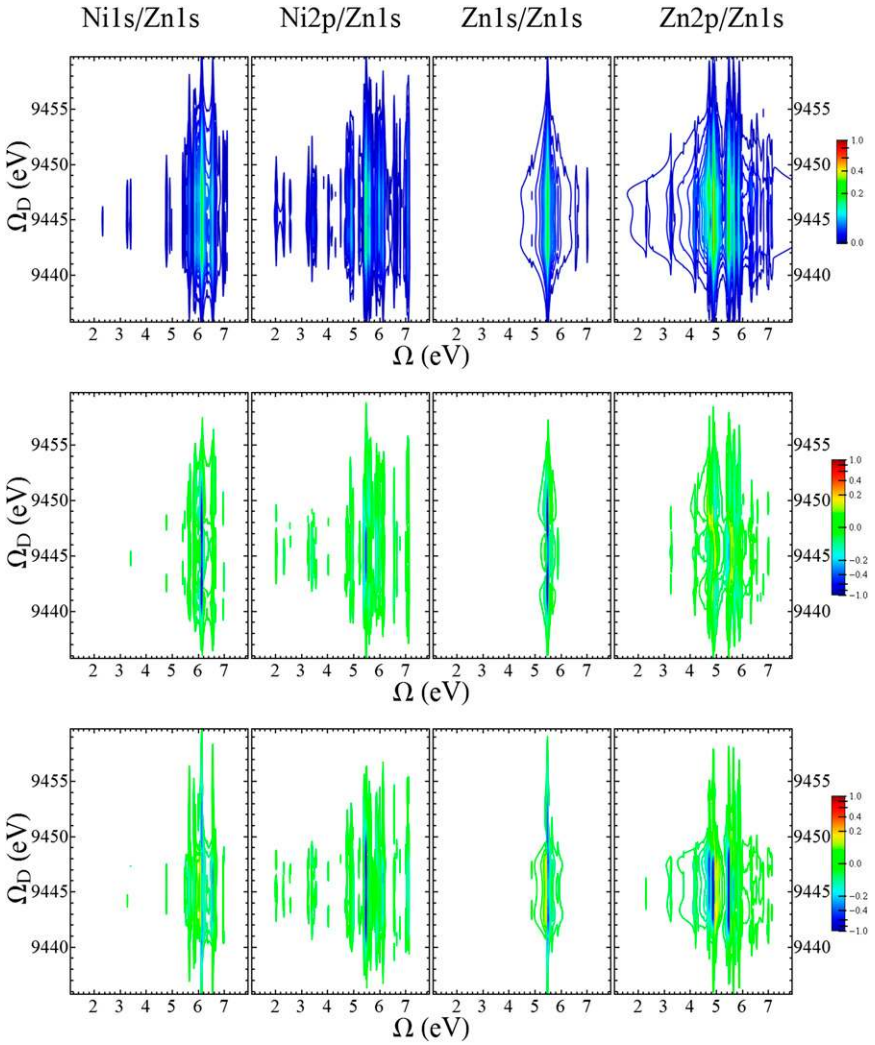

Fig. S8. The same as for Fig. S7 but with the probe tuned to the zinc K-edge.

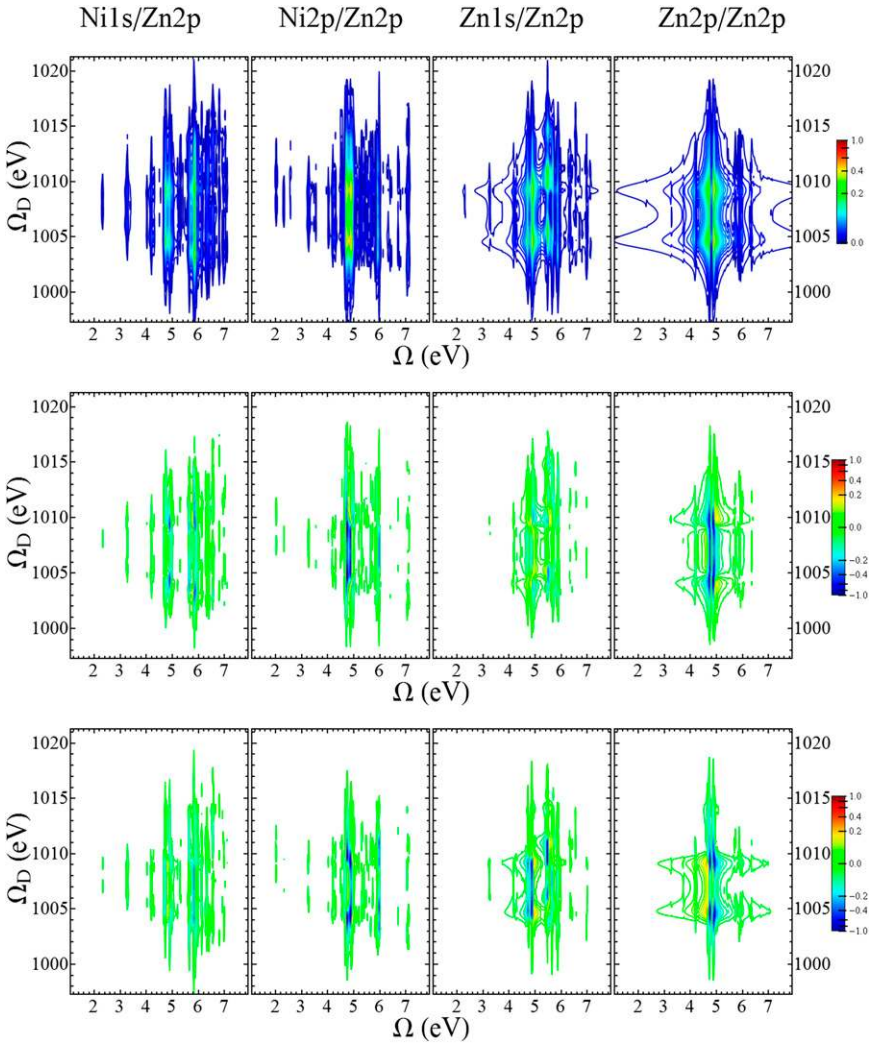

Fig. S9. The same as for Fig. S7 but with the probe tuned to the zinc L-edge.

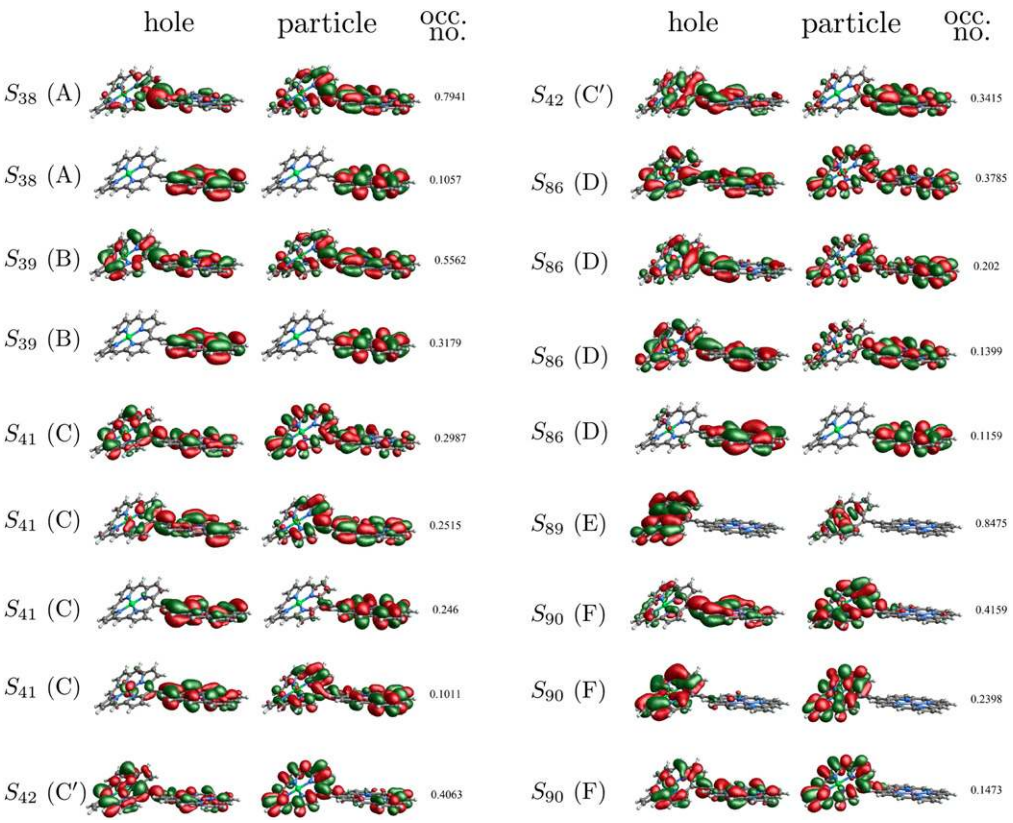

Fig. S10. Natural transition orbitals for the major peaks in the I2P-SXRS spectra shown in Fig. 3 of the main text. The occupation number is defined as w_ξ^2.

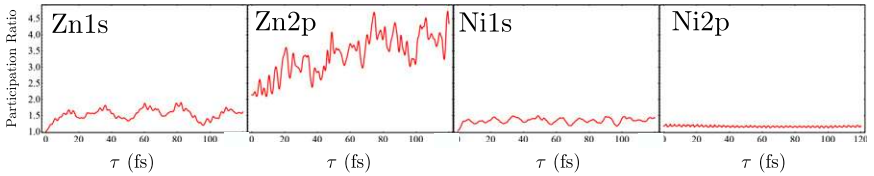

Fig. S11. Time-dependent participation ratios for valence wavepackets created by X-ray Raman excitation at the four core edges considered here, as indicated.

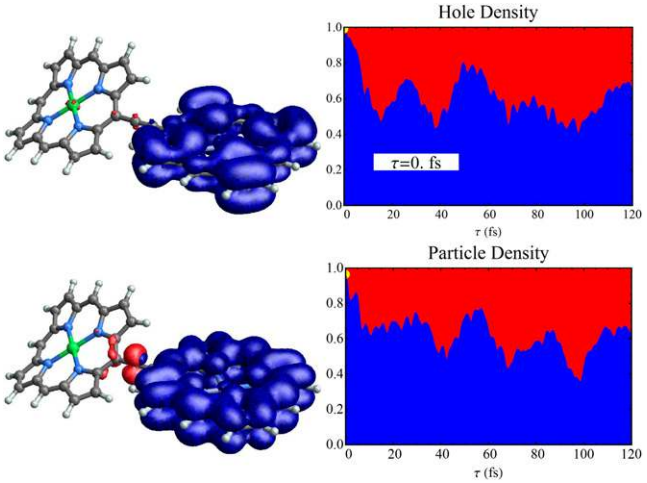

Movie S1. The electron and hole densities for the Zn2p doorway valence wavepacket for the first 120 fs following Raman excitation. (*Upper*) The reduced density for the hole. (*Lower*) The electron reduced density. (*Left*) Isosurfaces of the density, with red corresponding to the nickel monomer and blue to the zinc monomer. (*Right*) Plots of the integrated density, using the same color scheme. Initially, both electron and hole are entirely localized on the zinc monomer. Within 15 fs the hole is evenly delocalized between the monomers, following which there is coherent back and forth motion. The electron exhibits a similar trend, although the initial fast delocalization is not as complete.

Movie S1